Dalton Transactions

PAPER

View Article Online
View Journal | View Issue

Cite this: *Dalton Trans.*, 2018, **47**, 9834

The crystal structure and luminescence properties of a novel green-yellow emitting $Ca_{1.5}Mg_{0.5}Si_{1-x}Li_xO_{4-\delta}:Ce^{3+}$ phosphor with high quantum efficiency and thermal stability†

Weiwei Ji,[a] Zhiguo Xia,[b] Ke Liu,[a] Sayed Ali Khan,[a] Luyuan Hao,[a] Xin Xu,*[a] Liangjun Yin,[c] Maxim S. Molokeev,[d,e] Simeon Agathopoulos,[f] Wenyun Yang,[g] Xiaobai Ma,[h] Kai Sun[h] and Ivan da Silva[i]

Received 31st May 2018,
Accepted 2nd July 2018

DOI: 10.1039/c8dt02241k

rsc.li/dalton

A novel green-yellow emitting $Ca_{1.5}Mg_{0.5}Si_{1-x}Li_xO_{4-\delta}:Ce^{3+}$ phosphor with high quantum efficiency and thermal stability was discovered for applications in near ultraviolet pumped white light-emitting diodes. Its crystal structure was determined with a single-particle diagnosis approach. The Si sites in the SiO_4 tetrahedra are reported for the first time to accommodate Li^+ ions. This substitution, confirmed by ^6Li solid-state NMR and T.O.F. neutron powder diffraction, causes a disordered occupation of Ca/Mg in the $Ca_3MgSi_2O_8$ host and favors a phase transformation at ~330 °C, which results in the formation of the novel phosphor. The produced phosphor was efficiently excited by near UV light peaking at 365 and 410 nm and produced broad green-yellow emission with peaks at 500 and 560 nm, respectively. Its quantum efficiency reached 88.4% (internal) and 55.7% (external) under excitation at 365 nm, and 80.5% (internal) and 42.7% (external) under excitation at 410 nm, while the decrease of luminescence intensity at 200 °C was small (~26%). A WLED lamp with a high color rendering index of R_a = 92.8 was produced with the combination of a 365 nm emitting chip with blue emitting $BaMgAl_{10}O_{17}:Eu^{2+}$, green-yellow emitting CMSL:0.01Ce, and red emitting $Sr_2Si_5N_8:Eu^{2+}$ phosphors.

1. Introduction

Solid-state lighting technology based on phosphor-converted white light-emitting diodes (wLEDs or pc-wLEDs) has been attracting increasing interest nowadays because of its high efficiency, energy-saving features, quick response, long lifetime, compactness, and low negative environmental impact.[1–4] The commercial implementation scheme of WLEDs is generally based on the combination of InGaN-based blue LED chips with yellow $Y_3Al_5O_{12}:Ce^{3+}$ (YAG) phosphors.[5,6] Nevertheless, due to the intrinsic deficiency of green and red emissions of YAG phosphors, the CRI (color rendering index) of the resultant WLEDs is relatively low; hence, they do not satisfy the requirements for general lighting applications. A near ultraviolet (UV) LED (350–420 nm) coated with three-color (tricolor red, green, and blue) phosphors provided superior color uniformity with a high CRI and excellent quality of light.[7,8] Thus, they open up an excellent commercial prospect in the near future.

Green phosphor host compounds for near-UV LED are generally classified into oxynitrides, represented by $Si_{6-z}Al_zO_zN_{8-z}:Eu^{2+}$ and $(Ba,Sr,Ca)Si_2O_2N_2:Eu^{2+}$, and silicates, represented by $Ca_3Sc_2Si_3O_{12}:Ce^{3+}$ and $(Ba,Sr)_2SiO_4:Eu^{2+}$.[9–12] However, both of

[a]*Chinese Academy of Sciences Key Laboratory of Materials for Energy Conversion, Department of Materials Science and Engineering, University of Science and Technology of China, Hefei Anhui 230026, People's Republic of China. E-mail: xuxin@ustc.edu.cn; Fax: +86-551-63601592; Tel: +86-551-63600824(o), +86-18655117978(m)*
[b]*The Beijing Municipal Key Laboratory of New Energy Materials and Technologies, School of Materials Sciences and Engineering, University of Science and Technology Beijing, Beijing 100083, China*
[c]*School of Energy Science and Engineering, University of Electronic Science of China, 2006 Xiyuan Road, Chengdu, P.R. China*
[d]*Laboratory of Crystal Physics, Kirensky Institute of Physics, Federal Research Center KSC SB RAS, Krasnoyarsk 660036, Russia*
[e]*Department of Physics, Far Eastern State Transport University, Khabarovsk, 680021 Russia*
[f]*Department of Materials Science and Engineering, University of Ioannina, GR-451 10 Ioannina, Greece*
[g]*State Key Laboratory for Mesoscopic Physics, School of Physics, Peking University, Beijing 100871, P. R. China*
[h]*Department of Nuclear Physics, China Institute of Atomic Energy, Beijing 102413, P. R. China*
[i]*STFC-RAL, ISIS Facility, Harwell Science and Innovation Campus, Didcot, UK OX11 0QX*

†Electronic supplementary information (ESI) available. See DOI: 10.1039/c8dt02241k

them rather fail to produce high quantum efficiency (QE) and thermal stability at the same time. For instance, the $Si_{6-z}Al_zO_zN_{8-z}:Eu^{2+}$ phosphor exhibits high thermal stability, but it has a high production cost and lower QE compared to $Ba_2SiO_4:Eu^{2+}$. On the other hand, the $(Ba,Sr)_2SiO_4:Eu^{2+}$ phosphor suffers from severe thermal quenching.

The above examples suggest the need for developing novel phosphors with good thermal quenching properties and high quantum efficiency under excitation with UV-blue light. Intensive efforts have been recently focused on nitride phosphors with new crystal structures or compositions.[2,13–15,43] Takeda *et al.*[16] reported on a narrow-band green-emitting phosphor $Ba_2LiSi_7AlN_{12}:Eu^{2+}$ with high thermal stability. Nonetheless, the procedure followed to synthesize this nitride phosphor is expensive (high temperature and high pressure of N_2 are required).

Conventional environmentally-friendly silicate phosphors have been studied for many years, because of their high stability, easy synthesis process, and low production cost.[17–22] However, there has been no report on inventing any silicate phosphor with a new crystal structure for a long time. Ionic substitution (for example, Ba replaced by Sr in the $Ba_2SiO_4:Eu^{2+}$system) was often applied to control the luminescence properties of phosphors.[23,24] It has been reported that phase transformations rarely occur through this method,[18,19,21,25] (note that any other phase which might be developed is always known in the databases).

In this paper a novel orthosilicate $Ca_{1.5}Mg_{0.5}Si_{1-x}Li_xO_{4-\delta}:Ce^{3+}$ phosphor was successfully synthesized. The crystal structure of the new phosphor was thoroughly characterized, where Li^+ ions are reported for the first time to occupy the Si sites in the SiO_4 tetrahedra. Furthermore, the luminescence properties and the thermal stability under UV-blue light excitation were determined. The mechanism of production of this phosphor, which occurs *via* phase transformation from $Ca_3MgSi_2O_8$ to $Ca_{1.5}Mg_{0.5}Si_{1-x}Li_xO_{4-\delta}:Ce^{3+}$ at low temperatures, is discussed.

2. Materials and experimental procedures

Fine powders of $CaCO_3$, SiO_2, MgO, CeO_2, and Li_2CO_3 (Sinopharm Chemical Reagent Co. Ltd, Shanghai, China; purity 99.99%) were used. Powder mixtures (of the raw powders in a ratio to satisfy the stoichiometry of the phosphors) were thoroughly milled in a planetary ball mill in absolute ethanol media for 24 h and the produced homogeneous mixtures were dried at 100 °C in an oven in air. The dried powder mixtures were placed into alumina crucibles and fired at 1100–1300 °C for 6 h under a flowing N_2 + 0.5%H_2 atmosphere. After cooling, the products were ground and fired again at 1100–1300 °C for 6 h under the same atmosphere. The produced phosphors were directly characterized (*i.e.* with no further grinding process). The cooling rates were fixed to 2 K min^{-1}.

For the single-particle analysis, data collection was performed on a Bruker D8-Venture diffractometer with a Turbo X-ray source (Mo K_α radiation, λ = 0.71073 Å) adopting the direct drive rotating anode technique and a CMOS detector at room temperature. The data frames were collected using the program APEX2 and processed using the program SAINT routine in APEX2. The structures were solved by direct methods and refined by the full-matrix least squares on F^2 using the SHELXL-2014/7 program.[26] Solid-state luminescence and UV-vis-NIR spectra were recorded on a Craic Technologies microspectrophotometer. Crystals were placed on quartz slides under Krytox oil and data were collected after optimizing the microspectrophotometer. In order to determine the precise position of Li^+ ions, neutron powder diffraction (NPD) experiments were performed with a high resolution T.O.F. Fourier diffractometer HRFD [d-spacing range (0.6–3.6) Å, $\delta d/d \approx 0.1\%$] at the IBR-2 pulsed reactor in Dubna at room temperature. Rietveld refinements were carried out using TOPAS 4.2[27] over the d-spacing range (0.6–3.6) Å.

X-ray diffraction (XRD) analyses were done in Bragg–Brentano geometry using a Bruker D8 Advance diffractometer with a Cu $K\alpha_{1,2}$ radiation source (λ_1 = 1.54056 Å, λ_2 = 1.54439 Å) operated at 40 kV and 40 mA at a scanning rate of 1° min^{-1}, equipped with a Lynxeye XE detector. The morphology of the produced phosphors was observed by scanning electron microscopy (SEM, JED-2300, JEOL, Japan). Solid-state ^{6}Li NMR (MAS NMR) spectra were obtained on an AVANCE III 400 spectrometer using a 4 mm zirconia rotor spun at 15 kHz. The Larmor frequency and 90° pulse lengths for ^{6}Li were 58.9 MHz and 4.5 μs, respectively. The external reference for ^{6}Li was 1M aqueous LiCl. The emission and excitation spectra were recorded at room temperature with a fluorescence spectrophotometer (F-4600, Hitachi, Japan) with a 200 W Xe-lamp as an excitation source. The emission spectrum was corrected for the spectral response of a monochromator and Hamamatsu R928P photomultiplier tube (Hamamatsu Photonics K.K., Hamamatsu, Japan) using a light diffuser and tungsten lamp (Noma Electric Corp., NY; 10 V, 4A). The excitation spectrum was corrected for the spectral distribution of the xenon lamp intensity by measuring rhodamine-B as a reference.

The external (η_0) and internal (η_i) quantum efficiencies (QEs) were calculated using the following equations:[28]

$$\eta_0 = \frac{\int \lambda \cdot P(\lambda) d\lambda}{\int \lambda \cdot E(\lambda) d\lambda}; \quad \eta_i = \frac{\int \lambda \cdot P(\lambda) d\lambda}{\int \lambda \cdot \{E(\lambda) - R(\lambda)\} d\lambda} \tag{1}$$

where $E(\lambda)/h\nu$, $R(\lambda)/h\nu$, and $P(\lambda)/h\nu$ are the number of photons in the excitation, reflectance, and emission spectra of the phosphor, respectively. The QEs of the samples were evaluated using a quantum efficiency measurement system (QE-2100, Otsuka Electronics, Tokyo, Japan). The temperature-dependent luminescence was measured using an intensified multichannel spectrometer (MCPD-7000, Otsuka Electronics, Tokyo, Japan).

3. Results and discussion

3.1 Features of the novel crystal structure

The compound $Ca_{2.99}MgSi_2O_8$:0.01Ce^{3+} is a violet-blue emitting phosphor under UV light with a white body color.[29] As shown in the following paragraphs (Fig. 6d), a novel green-yellow light emitting phosphor was developed in the present work by replacing a small amount of Si with Li in $Ca_3MgSi_2O_8$. The photoluminescence properties of $Ca_{2.99}MgSi_2O_8$:0.01Ce^{3+} and the novel $Ca_{1.495}Mg_{0.5}Si_{0.88}Li_{0.12}O_4$:0.005$Ce^{3+}$ phosphor (denoted hereafter as CMSL:0.005Ce) are shown in comparison in the spectra of Fig. 1. The former phosphor shows a single emission band, which peaks at 410 nm under UV excitation at 326 nm. The latter phosphor was effectively excited by UV-blue light with the two highest peaks at 365 and 410 nm, and emits a strong green-yellow light with a peak at 500 nm.

This pronounced change in the luminescence spectra is attributed to phase transformation. The X-ray diffractograms of these phosphors are shown in Fig. 2. The diffractogram of the Li-free phosphor is a good match for the patterns of the phase of $Ca_3MgSi_2O_8$ (PDF card 35-0591). However, the X-ray diffractogram of CMSL:0.005Ce does not match the patterns of any known phase in the Inorganic Crystal Structure Database (ICSD).

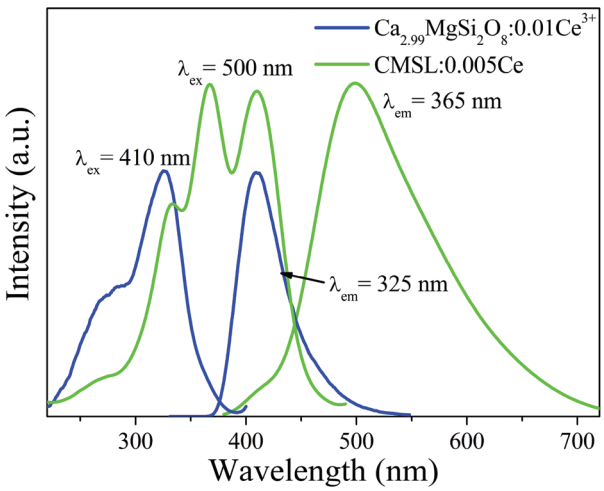

Fig. 1 Excitation and emission spectra of $Ca_{2.99}MgSi_2O_8$:0.01Ce^{3+} and CMSL:0.005Ce.

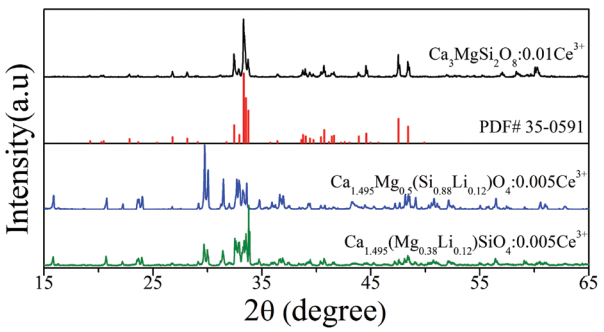

Fig. 2 X-ray diffractograms of the $Ca_3MgSi_2O_8$ with and without the doping of Li^+. The standard patterns of $Ca_3MgSi_2O_8$ (PDF card 35-0591) are also plotted.

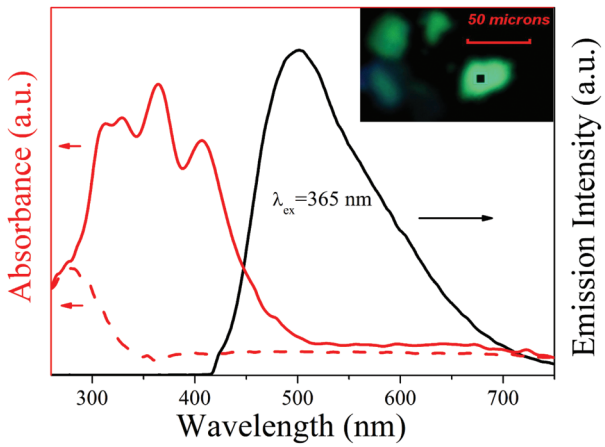

Fig. 3 Emission (λ_{ex} = 365 nm) and UV-Vis absorption spectra of the selected CMSL:0.005Ce particle, shown in the inset. The dashed line shows the UV-Vis absorption spectrum of a non-doped CMSL particle. The inset shows the photograph of a large green-emitting particle under 365 nm excitation.

Therefore, the single-particle diagnosis approach was applied to investigate the new unknown phase, as shown in Fig. 3. The inset of Fig. 3 shows a large green emitting particle under 365 nm excitation, which was selected for the analysis of the luminescence properties and crystal structure. The particle exhibited a broad absorption band from the UV to the deep blue region, which is in broad agreement with the excitation spectrum in Fig. 1. In conjunction with the absorption spectrum of the non-doped CMSL particle, this band can be ascribed to the allowed transition from 5d to 4f ($^2F_{7/2}$ and $^2F_{5/2}$) of the activator Ce^{3+} ion. The strong absorption at ~410 nm is a good match for the light green body color of CMSL:0.005Ce. As also shown in Fig. 3, the emission spectrum (λ_{ex} = 365 nm) is in accord with the emission of the phosphor powders (Fig. 1). Only the weak emission peak at ~410 nm in the phosphor powder disappears, which probably originated from the impurity $Ca_3MgSi_2O_8$:Ce^{3+} phase. The UV/Vis spectrum of a non-doped CMSL particle is also plotted in Fig. 3 with the dashed line, which exhibits a broad absorption band that peaks at 280 nm and a band gap of ~3.76 eV. No other absorption band was recorded, which is in accordance with the white body color.

The single crystal XRD analysis showed that the new phosphor has a monoclinic unit cell of a = 4.9978(6) Å, b = 6.6592(8) Å, c = 11.184(1) Å, and β = 90.575(4)°, with the $P2_1/m$ space group (No. 11). The crystal structure is similar to that of γ-Ca_2SiO_4 (as shown in Fig. S1†). If the angle β of the CMSL host changes from 90.575° to 90° and the fractional coordinates of all atoms remain unchanged, then its simulated XRD pattern is almost the same as that of γ-Ca_2SiO_4 (as shown in Fig. S2†); only the peaks slightly shift towards lower angles and some of them are overlapped.

The structure refinement was carried out by the least-squares minimization method using anisotropic thermal parameters for all atoms. There were two Si sites and four independent Ca sites in the structure. In the first stage, the Ca/Mg ratios in all Ca sites were refined assuming occupation (Ca) + occupation (Mg) = 1 in each site. Then, Li ion concentrations in the Ca/Mg sites were refined using the equation occupation (Ca) + occupation (Mg) + occupation (Li) = 1 in all sites. Unfortunately, this step of refinement was very unstable and even gave negative values for occupation (Li). Thus, Li ion concentrations were refined in all Si sites assuming the equation occupation (Si) + occupation (Li) = 1 and after working on this basis, the refinement was stable and gave non-zero values for the occupation (Li) in these sites. These results suggest that Li ions only occupy the Si sites in this system, which are coordinated with four oxygen atoms.

The chemical formula from the obtained crystal structure can be written as $Ca_{1.51(1)}Mg_{0.49(1)}Si_{0.925(5)}Li_{0.075(5)}O_4$, which is close to the formula suggested within 3σ. It should be noted that Si^{4+} replacement by Li^+ ions leads to a negative value of unit cell charge. Hence, O defects should appear and, therefore, the correct chemical formula is $Ca_{1.51(1)}Mg_{0.49(1)}Si_{0.925(5)}Li_{0.075(5)}O_{4-\delta}$.

The finally obtained crystal structure is depicted in Fig. 4. The crystal structure of $Ca_{1.51(1)}Mg_{0.49(1)}Si_{0.925(5)}Li_{0.075(5)}O_{4-\delta}$ was built up of isolated $(Si,Li)O_4$ tetrahedra (Fig. 4a and b), which is the typical structure for orthosilicates. Columns of edge-sharing $(Ca,Mg)O_6$ octahedra run along one axis and are held together by corner- and edge-sharing $(Ca,Mg)O_6$ octahedra and $(Si,Li)O_4$. The crystal data and atomic coordinates along with the isotropic displacement parameters are shown in Tables 1 and 2, respectively. The anisotropic atomic displacement parameters and the selected interatomic distances are listed in Tables S1 and S2,† respectively. Further details of the crystal structure may be obtained from Fachinformationszentrum Karlsruhe on quoting the deposition number CSD-431225 and the ESI† included in the CIF file.

The framework of $Ca_{1.51(1)}Mg_{0.49(1)}Si_{0.925(5)}Li_{0.075(5)}O_{4-\delta}$ hosts four crystallographically independent $Ca^{2+}(Mg^{2+})$ ions (marked as A_1, A_2, B_1, B_2) (Fig. 4c) with the same coordination number of six. A_1 and A_2 have an inversion symmetry, corresponding to the A site in γ-Ca_2SiO_4, while B_1 and B_2 have mirror asymmetry, corresponding to the B site in γ-Ca_2SiO_4 (A and B sites in γ-Ca_2SiO_4 are shown in Fig. S3†). The coordinate spheres of the four sites are shown in Fig. 4c. The average coordination distance increases in the sequence A_1 (2.241 Å), A_2 (2.332 Å), B_1 (2.372 Å), B_2 (2.388 Å), and the distortion of the octahedral increases in the same order due to the scattering of the coordination distance and bond angle.

The actual composition is slightly different from the starting powder composition of $Ca_{1.5}Mg_{0.5}(Si_{0.88}Li_{0.12})O_4$:0.005$Ce^{3+}$, possibly on account of the evaporation of Li at high temperatures, as shown in the TGA curve in Fig. S4.† However, to maintain a consistency on paper, the nominal composition of the starting powder mixture is used in the following sections.

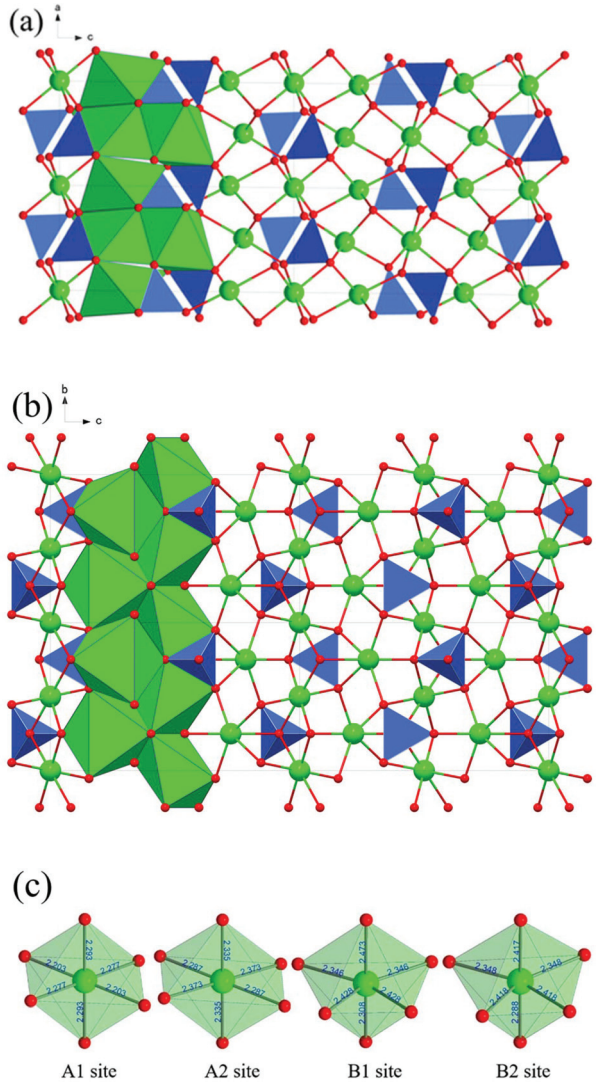

Fig. 4 Crystal structure of CMSL:0.005Ce, (a) from the [010] direction, and (b) the [001] direction, and (c) coordinate polyhedra of four kinds of (Ca,Mg) in CMSL:0.005Ce. The blue tetrahedra correspond to $(Si,Li)O_4$ and the green octahedra to $(Ca,Mg)O_6$. The green spheres correspond to Ca or Mg, and the red spheres to O.

The produced phosphor was actually a mixture of CMSL and $Ca_3MgSi_2O_8$ phases, as shown in Fig. 5; (in the final product, the CMSL phase, calculated by the profile fitting analysis of the XRD patterns in Fig. 5, was ~87%).

It is noteworthy that the $LiO(N)_4$ tetrahedra can be found in silicates and nitridosilicates,[16,30] but no paper reports on the Li replacement of Si in the SiO_4 tetrahedra. It was originally believed that Li occupies the Mg site owing to the similar bonding properties between Mg and Li. However, the XRD results for the composition $Ca_{1.495}(Mg_{0.38}Li_{0.12})SiO_4$:0.005$Ce^{3+}$ (Fig. 2) suggest that when Mg is replaced by Li, the obtained phosphor contains a higher amount of impurity phase than the sample where Li replaced Si.

The ^{6}Li MAS NMR spectrum of silicates is dominated by chemical shift effects and has high resolution, which allows

Table 1 Crystallographic data of $Ca_{1.51(1)}Mg_{0.49(1)}Si_{0.925(5)}Li_{0.075(5)}O_{4-\delta}$

Crystal system	Monoclinic
Space group	$P2_1/m$
Cell parameters/Å	a = 4.9978(6), b = 6.6592(8), c = 11.184(1)
β/°	90.575(4)
V/Å^3	372.19(8)
Z	4
Radiation type	Mo K_α
Absorption coefficient	2.629
Crystal size/μm	40 × 30 × 20
Diffractometer	Bruker D8-Venture diffractometer
Abs correction	Multiscan
Measured reflections	6097
Independent reflections	933
Observed reflections	764
R_{int}	0.0371
$R[F^2 > 2\sigma(F^2)]$	0.0393
$wR(F^2)$	0.0457
S	1.064
$\Delta\rho_{max}$, $\Delta\rho_{min}$/e Å^{-3}	0.458, −0.490

Table 2 Atomic coordinates, occupancies, and isotropic atomic displace parameters of $Ca_{1.51(1)}Mg_{0.49(1)}Si_{0.925(5)}Li_{0.075(5)}O_{4-\delta}$

Atom	x	y	z	$U_{eq.}$ (Å)	Occupancy
Ca1	0	0	0	0.0042(3)	0.45(1)
Mg1	0	0	0	0.0042(3)	0.55(1)
Ca2	1/2	0	1/2	0.0092(3)	0.84(1)
Mg2	1/2	0	1/2	0.0092(3)	0.16(1)
Ca3	0.4867(1)	1/4	0.21618(6)	0.0051(2)	0.87(1)
Mg3	0.4867(1)	1/4	0.21618(6)	0.0051(2)	0.13(1)
Ca4	0.0135(1)	1/4	0.72373(6)	0.0089(3)	0.87(1)
Mg4	0.0135(1)	1/4	0.72373(6)	0.0089(3)	0.13(1)
Si1	0.9267(2)	1/4	0.40276(8)	0.0055(3)	0.922(6)
Li1	0.9267(2)	1/4	0.40276(8)	0.0055(3)	0.078(6)
Si2	0.5798(2)	1/4	0.91159(8)	0.0099(4)	0.926(6)
Li2	0.5798(2)	1/4	0.91159(8)	0.0099(4)	0.074(6)
O1	0.2509(4)	1/4	0.4038(2)	0.0109(5)	1
O2	0.2547(5)	1/4	0.9179(2)	0.0180(6)	1
O3	0.7295(4)	1/4	0.0439(2)	0.0145(6)	1
O4	0.8021(4)	1/4	0.5393(2)	0.0139(6)	1
O5	0.7930(3)	0.0536(3)	0.3374(1)	0.0111(4)	1
O6	0.7098(3)	0.4462(3)	0.8451(1)	0.0160(4)	1

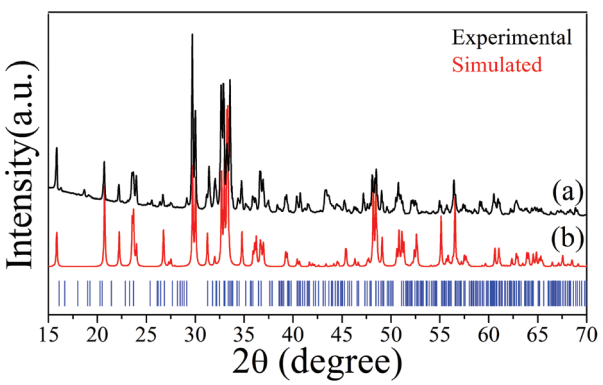

Fig. 5 X-ray diffractograms of the CMSL:0.005Ce fine powder experimentally recorded (a), and calculated by a simulation based on the structural parameters of the single XRD analysis (b). The peak positions of the impurity phase of $Ca_3MgSi_2O_8$ are marked with the blue ticks.

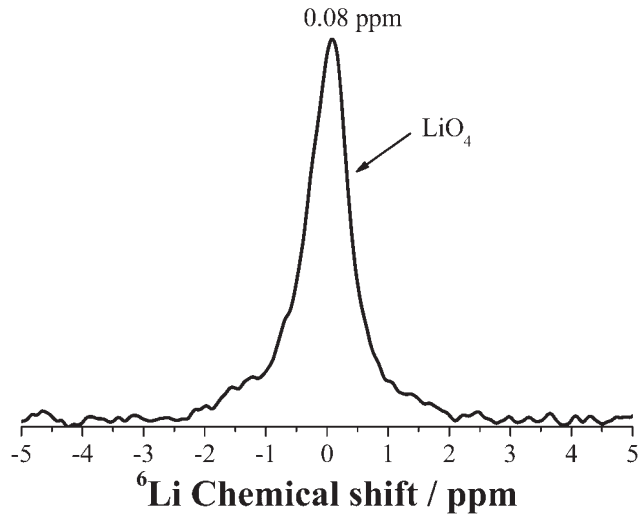

Fig. 6 ^{6}Li MAS NMR spectrum of ^{6}Li in CMSL:0.005Ce (spin speed = 15.0 kHz).

one to obtain significant structure information.[31] To be more specific, the spectrum of CMSL:0.005Ce (Fig. 6) presents a single peak at 0.08 ppm with a FWHM of 30 Hz. The ^{6}Li peak position of the four-coordinated Li (LiO_4) is located at 0.09–0.2 ppm with a FWHM of 10–20 Hz, while the ^{6}Li peak position of the six-coordinated Li (LiO_6) is located at −1.0 ~ −0.6 ppm.[31–33] Thus, the NMR signal at 0.08 ppm suggests that Li occupies the four-coordinated Si sites. The possibility of the replacement of Si in the SiO_4 tetrahedra by Li will be further confirmed by the neutron diffraction process and will be discussed later.

3.2 Phase transformation of CMSL:Ce at low temperatures

The appearance and the morphology of the produced phosphors, summarized in Fig. 7, revealed very interesting features. In particular, when the sample of the CMSL:0.005Ce phosphor was taken out of the furnace at ~400 °C, it appeared as a very hard sintered lump, and its color was white under ambient light and blue under UV (365 nm) light excitation, as shown in Fig. 7a and c, respectively. When the temperature decreased at ~330 °C, that lump spontaneously cracked into a soft fine

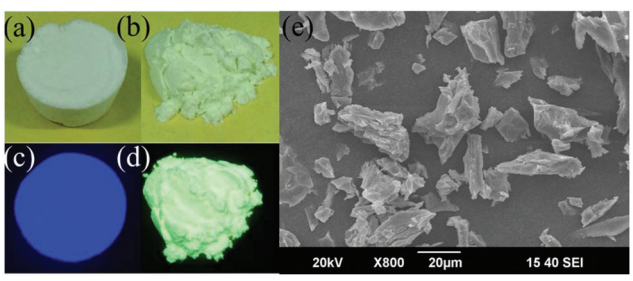

Fig. 7 Photographs of the CMSL:0.005Ce phosphor at 400 °C (a, c) and at room temperature (b, d) under ambient light (a, b) and UV (365 nm) light (c, d), and (e) SEM image of the particles of the as-received powder of the phosphor.

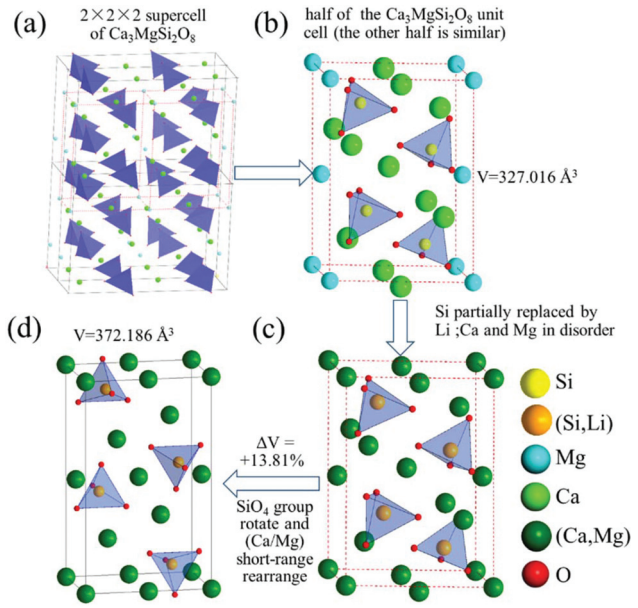

Fig. 8 The diagram of the phase transformation from $Ca_3MgSi_2O_8$ to CMSL.

powder, attributed to a volume expansion (explained later in Fig. 8) due to the phase transformation occurring at this temperature, which is similar to γ-Ca_2SiO_4:Ce phosphors.[21,34] Thermal analysis (DSC, Fig. S4†) also recorded a sudden temperature difference at this point, which confirms the phase transformation. Moreover, the particles of the powder had a lath-like morphology with many cracks (Fig. 7e), which further support the above statements. The phosphor at room temperature was light green under ambient light and bright green under UV (365 nm) light excitation, as shown in Fig. 7b and d, respectively.

The phase transformation from $Ca_3MgSi_2O_8$ to CMSL is schematically depicted in Fig. 8. A representative unit (Fig. 8b) was taken out from the supercell of the $Ca_3MgSi_2O_8$ crystal (Fig. 8a). There are three Ca sites and one Mg site in Fig. 8b, which correspond to the four Ca/Mg sites in CMSL. At high temperatures, Li enters Si sites and Ca and Mg both enter each other's sites partially, which generates the disordered structure of $Ca_3MgSi_2O_8$ (Fig. 8b → Fig. 8c). Then, the SiO_4 tetrahedra rotate and move over a short distance, and Ca/Mg ions move over a short distance simultaneously (Fig. 8c → Fig. 8d), which result in the phase transformation from $Ca_3MgSi_2O_8$ to CMSL. A volume expansion of 13.81% occurs in this phase transformation. It is noteworthy that this process is impossible for the $Ca_3MgSi_2O_8$ host but easily occurs when some Si ions are replaced by Li ions.

When the CMSL:0.005Ce samples were naturally cooled to room temperature inside the furnace, an uncracked (untransformed) thin layer was often detected on the surface of the fine powder, which emitted blue light under the excitation of UV light. The single-particle diagnosis approach suggested that it had a composition of $Ca_3MgSi_{1.961(6)}Li_{0.039(6)}O_8$, which means that Li ions still occupy Si sites, while Ca and Mg are distributed in an orderly manner in the $Ca_3MgSi_2O_8$ host (Tables S3 and S4†). The lower Li concentration is ascribed to the evaporation of Li from the surface of the sample (Fig. S4†). Further details of the crystal structure may be obtained from Fachinformationszentrum Karlsruhe on quoting the deposition number CSD-431226 and the ESI† included in the CIF file.

Neutron diffraction profiles include useful information on lithium, because the scattering ability of the lithium nucleus (amplitude of the coherent scattering length) is relatively large and independent of the scattering vector $Q = 4\pi \sin\theta/\lambda$.[35] This makes it possible to distinguish lithium from other elements easily, in contrast to the negligible X-ray scattering ability of lithium or lithium ions.

Unfortunately, the novel CMSL phase is very difficult to achieve a highly-pure phase (Fig. 5). The untransformed thin layer on the surface consisted of the pure $Ca_3MgSi_2O_8$ phase. Therefore, the untransformed pure $Ca_3MgSi_2O_8$:Li phase was selected to conduct neutron diffraction analysis in order to determine the location of Li in this system. To make the refinement process easier and more reliable, no Ce ions were added.

Rietveld refinement was performed by using TOPAS 4.2.[27] Almost all peaks were indexed to the monoclinic unit cell ($P2_1/c$) with parameters close to $Ca_3MgSi_2O_8$. There are two Si sites in the asymmetric part of the unit cell. The model of the crystal structure accounts Li ions in these positions, and Li/Si occupations were refined on the assumption that the sum of occupancies occ(Si) + occ(Li) = 1. The Rietveld refinement pattern for time-of-flight neutron diffraction data measured at room temperature for $Ca_3MgSi_2O_8$:Li is shown in Fig. 9. The quality of the refinement is satisfactory and gives low R-factors (R_{wp} = 3.4%, R_{exp} = 2.44%, χ^2 = 1.40) (Table S5†).

The atomic coordinates along with the isotropic displacement parameters of $Ca_3MgSi_2O_8$:Li are shown in Table 3. It

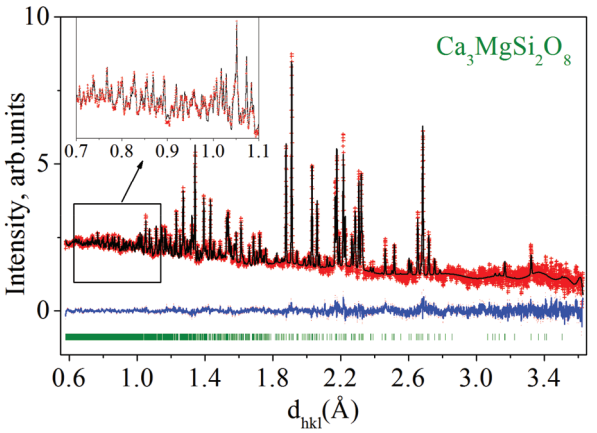

Fig. 9 T.O.F. neutron powder diffraction data of $Ca_3MgSi_2O_8$:Li. The observed and the Rietveld calculated curves are plotted. The third curve depicts the difference in the intensity between the aforementioned curves. The peak positions of the $Ca_3MgSi_2O_8$ phase are marked with the green ticks.

Table 3 Fractional atomic coordinates and isotropic displacement parameters (Å^2) of $Ca_3MgSi_2O_8$:Li

	X	*y*	*z*	B_{iso}	Occ.
Ca1	0.2256(6)	0.1812(8)	0.2547(6)	3.4(1)	1
Ca2	−0.0640(6)	0.229(1)	0.0856(5)	3.0(1)	1
Ca3	0.4118(9)	0.735(2)	0.0937(7)	5.5(2)	1
Mg	0.2524(7)	0.252(2)	0.0031(5)	2.90(7)	1
Si1	0.5971(7)	0.230(1)	0.1328(5)	1.9(2)	0.98(2)
Li1	0.5971(7)	0.230(1)	0.1328(5)	1.9(2)	0.02(2)
Si2	0.0938(8)	0.729(2)	0.1411(7)	3.2(2)	0.94(3)
Li2	0.0938(8)	0.729(2)	0.1411(7)	3.2(2)	0.06(3)
O1	0.4445(7)	0.216(1)	0.0772(6)	4.3(1)	1
O2	0.6903(6)	0.425(1)	0.0641(4)	4.0(1)	1
O3	0.6740(5)	−0.0482(9)	0.1248(4)	2.62(8)	1
O4	0.5967(6)	0.3612(9)	0.2398(4)	3.43(9)	1
O5	−0.0551(6)	0.701(1)	0.0751(5)	3.5(1)	1
O6	0.0647(5)	0.8201(9)	0.2555(4)	3.33(9)	1
O7	0.1867(6)	0.481(1)	0.1260(5)	4.2(1)	1
O8	0.1768(6)	−0.053(1)	0.0833(4)	3.6(1)	1

can be observed that Li ions occupy Si1 and Si2 sites simultaneously, which is consistent with the above single-crystal X-ray diffraction results of $Ca_3MgSi_2O_8$ (Table S4†), and confirms that Li could also substitute Si in the SiO_4 tetrahedra of the novel phosphor.

Based on the results of ^{6}Li MAS NMR of CMSL, T.O.F. neutron powder diffraction of $Ca_3MgSi_2O_8$:Li, and the single-crystal X-ray diffraction of $Ca_3MgSi_2O_8$ and CMSL, one can reach the conclusion that Li ions definitely occupy the Si sites in this system. It is generally accepted that the replacement of Si^{4+} by Li^+ is impossible, owing to the huge gap between the ion radius of Si^{4+} (26 pm) and that of Li^+ (59 pm).[36] No ion has a sharp boundary, and there are several different measures of ionic radii in use based on different assumptions. The most acceptable ionic radii table was reported by Shannon using a value of $r_{ion}(O^{2-})$ = 140 pm.[36] In fact, if the positive ion is small and/or highly charged, it will distort the electron cloud of the negative ion, leading to a build-up of extra charge density between the two nuclei, *i.e.*, to partial co-valency. This will decrease the anion radius and the calculated cation radius is underestimated if the anion radius is set to a fixed value.[36] For example, the radii of B^{3+}, C^{4+}, H^+, and N^{5+} are 0.01 Å (3), −0.08 Å (4), −0.38 Å (1), and −0.104 Å (3) in that table, respectively, and the inference is that the ionic radius of Si^{4+} has been seriously underestimated.[36] In contrast, in our opinion, both Si–O and Li–O have covalent characteristics,[37,38] and the covalent radii of Li and Si are 128 and 111 pm, respectively,[39] whose difference is not as big as that of the ionic radii. This makes it possible to replace part of the amount of Si with Li.

The main bond lengths of $Ca_3MgSi_2O_8$:Li are presented in Table S6.† The chemical formula for the obtained crystal structure can be written as $Ca_3Mg(Si_{1.92(3)}Li_{0.08(3)})O_8$. It should be noted that Si replacement by Li leads to a negative value of unit cell charge; hence, O defects should appear and the correct chemical formula is $Ca_3Mg(Si_{1.92(3)}Li_{0.08(3)})O_{8-\delta}$, where δ = 0.12 in the case investigated in the present study.

According to Fig. 4c and Table 2, Ca and Mg simultaneously occupy all the four Ca/Mg sites in CMSL. This suggests that Ca and Mg have already been in a disorder regime in the $Ca_3MgSi_2O_8$ phase at high temperatures (Fig. 8c). It is worth noting that the low temperature phase transformation ordinarily occurs through a short-range rearrangement of the coordinated structure without breaking any bond.[40] Consequently, Li incorporation seemingly favors the disordered occupation of Ca and Mg. The phase of $Ca_3MgSi_2O_8$, with disordered Ca/Mg occupation, transforms very easily into the novel CMSL phase, which is proved by the sudden temperature difference shown in Fig. S4.† It seems that the cooling rate has a negligible influence on this phase transformation. For instance, when the hot lump was quenched by rapid immersion in cold water or carbon tetrachloride, most of the powder was still transformed into CMSL.

3.3. Luminescence properties and applications

The photoluminescence (PL) properties were studied with a series of $Ca_{1.995-x}Mg_xCe_{0.005}Si_{0.88}Li_{0.12}O_4$ phosphors, produced with different values of *x*, and their X-ray diffractograms are plotted in Fig. 10. Only the γ-Ca_2SiO_4 phase was developed for the samples with $x \leq 0.2$. Since the XRD patterns of the two phases (γ-Ca_2SiO_4 and $Ca_3MgSi_2O_8$) are similar, the focus of attention was placed on the intensity of the peak of the plane $(111)_\gamma$ of γ-Ca_2SiO_4 to record the presence of this phase. With the increase of the *x* value, the intensity of this peak gradually decreased and disappeared when *x* was 0.5, suggesting that γ-Ca_2SiO_4 does not form in this value of *x*. When *x* values were 0.3 and 0.4, the produced phosphors were mainly mixtures of CMSL and γ-Ca_2SiO_4, which is also evident from the emission spectra under UV light (shown later in Fig. 11a). The amount of the impurity phase of $Ca_3MgSi_2O_8$ increased when *x* was higher than 0.5, and it was predominantly formed in the sample with *x* = 0.7.

The emission spectra of $Ca_{1.995-x}Mg_xCe_{0.005}Si_{0.88}Li_{0.12}O_4$ phosphors with different *x* values under excitation at 365 nm

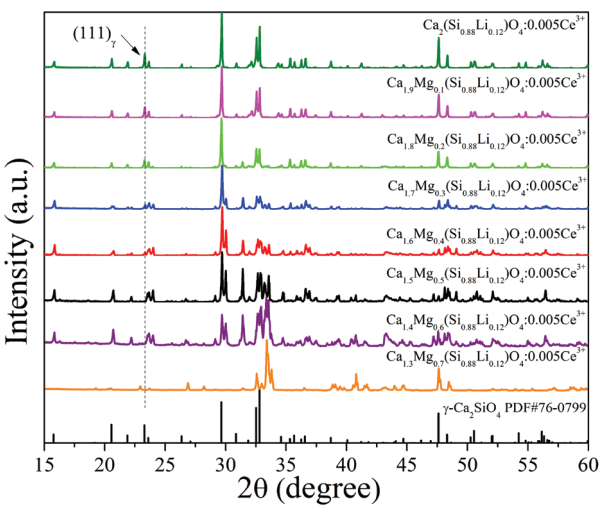

Fig. 10 X-ray diffractograms of $Ca_{1.995-x}Mg_xCe_{0.005}Si_{0.88}Li_{0.12}O_8$. The patterns of γ-$Ca_2SiO_4$ are also plotted. The $(\phi 111)_\gamma$ peak of γ-Ca_2SiO_4 is marked.

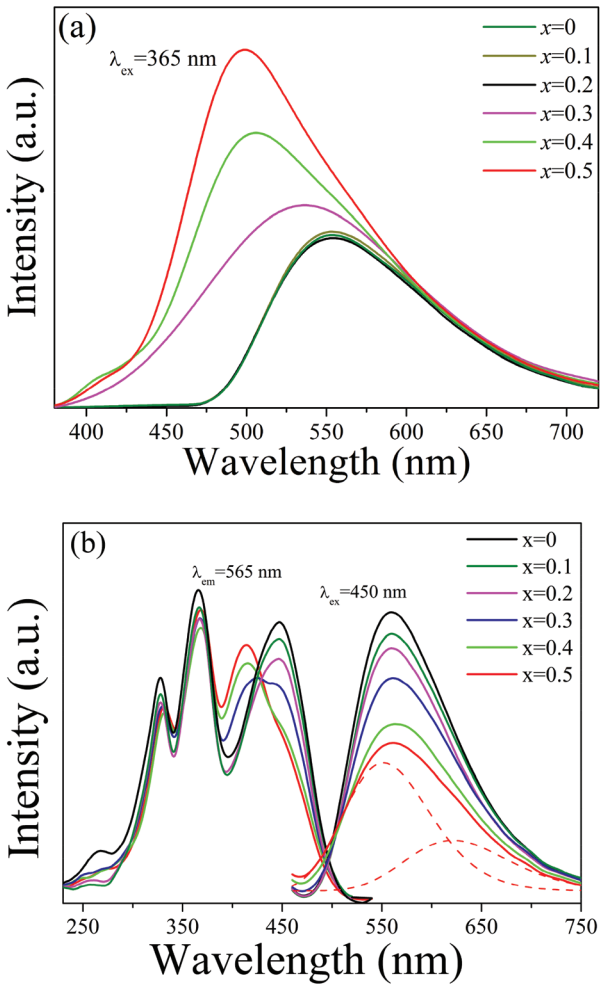

Fig. 11 PL spectra of $Ca_{1.995-x}Mg_xCe_{0.005}Si_{0.88}Li_{0.12}O_8$ phosphors, (a) emission spectra under excitation at 365 nm, and (b) excitation spectra monitored at 565 nm and emission spectra under excitation at 450 nm. The approximate spin–orbit splitting of the emission band of CMSL:0.005Ce is represented by the two red dashed curves centered at 552 and 621 nm.

are shown in Fig. 11a. For $x = 0$, the emission band peaked at 560 nm and originated from pure γ-Ca_2SiO_4:0.005Ce^{3+}.[21] With the increase of x value, a new emission band with a peak at ~500 nm and with an increasing intensity was recorded. It is noteworthy that the emission band of the CMSL:0.005Ce phosphor, further in the green emission region, also covers the emission region of γ-Ca_2SiO_4:0.01Ce^{3+}. This means that the QE of CMSL:0.005Ce is much higher than that of γ-Ca_2SiO_4:0.01Ce^{3+}, because 365 nm is also the excitation peak of Ca_2SiO_4:0.005Ce^{3+}, as shown in Fig. 11b.

The excitation spectra monitored at 565 nm and the emission spectra under excitation at 450 nm for $Ca_{1.995-x}Mg_xCe_{0.005}Si_{0.88}Li_{0.12}O_4$ phosphors are plotted in Fig. 11b. The excitation spectrum of CMSL:0.005Ce is similar to that monitored at 500 nm. The increase of x value does not cause any shift in the wavelength of the emission peak but its intensity decreases. The CMSL:0.005Ce phosphor for $x = 0.5$ emits yellow light at ~560 nm, which can be de-convoluted into two Gaussian bands with peaks at 552 and 621 nm. Their energy difference is ~2029 cm^{-1}, which is close to the ^2F_J (J = 7/2, 5/2) energy gap of Ce^{3+} (~2000 cm^{-1}) in most Ce^{3+} activated phosphors. This suggests that the emission at ~560 nm originates from single Ce^{3+} lattice sites in CMSL:0.005Ce.

The influence of Ce content on the excitation and emission spectra of CMSL:yCe phosphors is shown in Fig. 12. A broad emission band was recorded, whose FWHM increases in addition to red-shifting with the increase of y value apparently on account of the increase of yellow emission. The emission band was de-convoluted into four Gaussian bands with peaks at 490, 536, 552, and 621 nm. The energy difference between the two high energy peaks is ~1750 cm^{-1} and for the two low energy peaks it is ~2029 cm^{-1}, which suggests that the emission band in these phosphors derives from two kinds of emission centers: one center emits green light (~500 nm) and the other center emits yellow light (~560 nm). The fact that the energy difference between the two high energy peaks is a little lower than that between the two low energy peaks is attributed to the re-absorption of the high energy emission by the Ce^{3+} emitting yellow light. In fact, all the emission bands can be de-convoluted into four Gaussian bands with similar peak wavelengths regardless of the Ce content.

The low-temperature emission spectra of CMSL:0.005Ce were also obtained (Fig. S5†). It is observed that the emission intensity increased with the decrease of temperature, but the shape of the emission spectra remains almost the same, which confirms that the two emission centers come from one phase, and not a mixture.

It has already been mentioned that the crystal structure of CMSL is similar to γ-Ca_2SiO_4. Based on first-principles calculations and photoluminescence properties, we have reported in an earlier study that Ce^{3+} ions are prone to occupy the A sites in the γ-Ca_2SiO_4 phosphor.[21] Since the A_1 and A_2 sites in CMSL

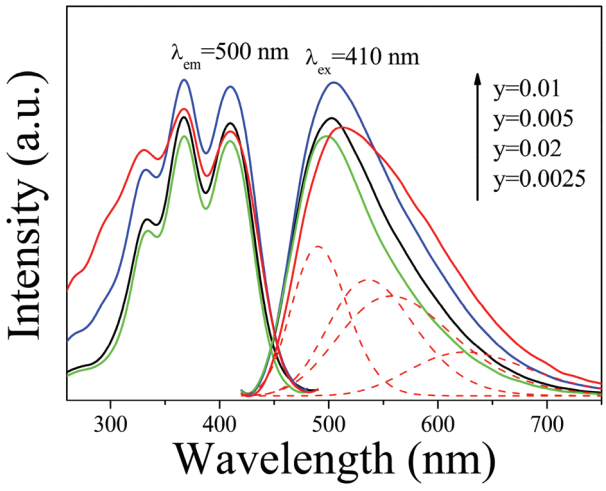

Fig. 12 PL excitation and emission spectra of CMSL:yCe phosphors. The emission band of CMSL:0.02Ce is de-convoluted into four Gaussian bands (red dashed lines).

correspond to the A sites in γ-Ca_2SiO_4, it is reasonably proposed that Ce ions occupy the A_1 and A_2 sites. Due to the lower average coordination distance and the lower distortion of coordination of the octahedra in the A_1 sites, the crystal field around the A_1 sites is stronger than that around the A_2 sites. Consequently, the green emission originates from Ce^{3+} in the A_2 sites and the yellow emission originates from Ce^{3+} in the A_1 sites.

The occupancy of Ca ions is 0.45 and 0.84 in the A_1 and A_2 sites, respectively, because these are originally Mg and Ca sites in $CaMgSi_2O_8$, respectively; thus, Ca should prefer to occupy its own positions. For the coordination number (CN) = 6, the ionic radii are 101 pm for Ce^{3+}, 100 pm for Ca^{2+}, and 72 pm for Mg^{2+}. Due to the similar ionic radii, Ce^{3+} prefers to occupy the Ca^{2+} sites, because the occupancy of Ca is much higher in the A_2 sites. Ce^{3+} prefers to occupy the A_2 sites, which results in a stronger green emission rather than yellow emission. The increase of Ce^{3+} content causes an increase of the occupancy in the A_1 sites with Ce ions, which leads to the increase of yellow emission.

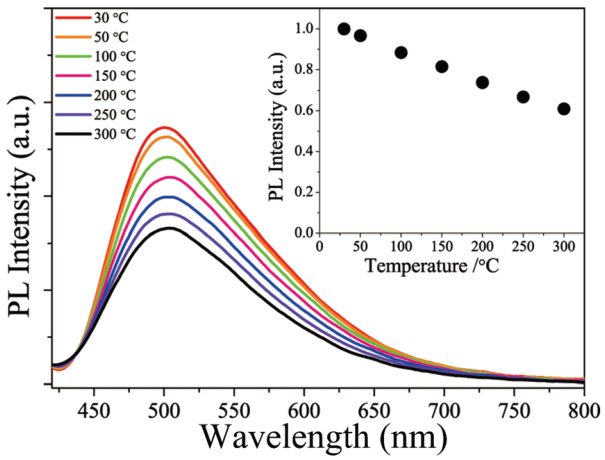

Fig. 13 Temperature dependence of the emission spectra of the CMSL:0.01Ce phosphor under the excitation of 410 nm. The peak intensity is shown in the inset.

The increase of temperature caused a decrease of emission intensity; more specifically, the peak intensities at 200 and 300 °C were 73.8% and 60.1% of the intensity observed at room temperature, respectively (Fig. 13). The produced phosphors generally have better thermal stability compared to conversional green $Ba_2SiO_4:Eu^{2+}$ phosphors, where less than 20% of the intensity at room temperature was retained at 200 °C, and is similar to $Si_{6-z}Al_zO_zN_{8-z}:Eu^{2+}$ and $Ca_3Sc_2Si_3O_{12}:Ce^{3+}$green phosphors.[10,41] It is noteworthy that almost all Ce ions in the CMSL:0.01Ce phosphor are Ce^{3+} (Fig. S6,† Ce LIII-edge XANES spectrum).

The QE of the produced CMSL:0.01Ce phosphor was measured. The internal and external QE are 88.4% and 55.7%, respectively, under 365 nm excitation and 80.5% and 42.7%, respectively, under 410 nm excitation. These QE values are much higher than 47% (internal) and 30% (external) of the Al doped γ-$Ca_2SiO_4:Ce^{3+}$ phosphor (450 nm excitation),[18] and comparable to $Si_{6-z}Al_zO_zN_{8-z}:Eu^{2+}$ (405 nm excitation, 41% (external))[10,41] and $Ca_3Sc_2Si_3O_{12}:Ce^{3+}$ (450 nm excitation, 41.2% (external))[9,42] green phosphors. The last two materials are commercially available now.

In order to generate white light and fabricate a LED device, a 365 nm chip with blue-emitting $BaMgAl_{10}O_{17}:Eu^{2+}$, green-yellow emitting CMSL:0.01Ce, and red-emitting $Sr_2Si_5N_8:Eu^{2+}$ phosphors was used (inset of Fig. 14a). The electroluminescence (EL) spectrum of the obtained LED driven under a 30 mA forward bias current is shown in Fig. 14a. The CIE color coordinates, the correlated color temperature (T_c), and the average color rendering index R_a were (0.335, 0.360), 5423 K, and 92.8, respectively. LED devices using a 410 nm chip with green-yellow emitting CMSL:0.01Ce and red-emitting $Sr_2Si_5N_8:Eu^{2+}$ phosphors were also fabricated. The EL spectrum of the obtained LED driven under a 30 mA forward bias current is shown in Fig. 14b and the above three properties were (0.353, 0.333), 4600 K, and 90.4, respectively. The full sets of 15 CRIs with the color rendering index for both WLEDs are listed in Table S7.†

The novel phosphor displays excellent potential for applications in white LEDs. Nevertheless, the production of pure

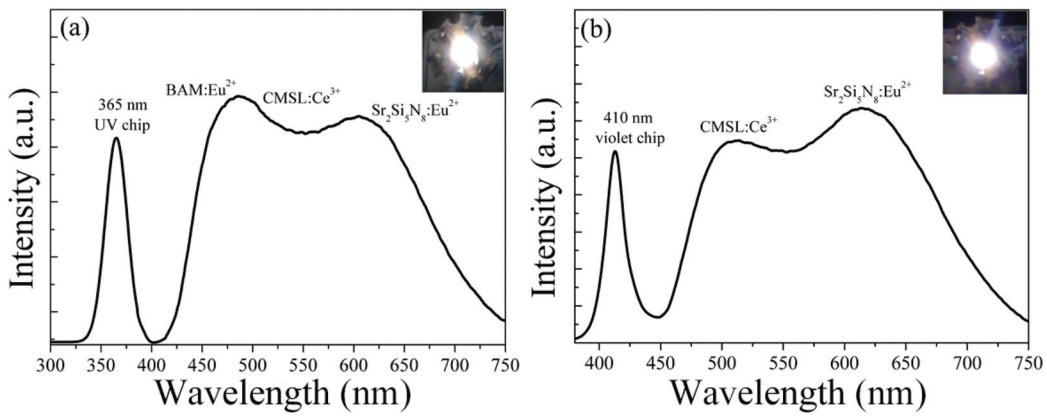

Fig. 14 EL spectra of WLEDs based on a (a) 365 nm chip and a (b) 410 nm chip. The insets show the photographs of the corresponding LED packages.

CMSL:Ce, which will feature a broad FWHM and considerably higher QE is still a challenge. On account of the large difference between the internal and the external QE, methods for improving surface modification should be discovered in order to enhance the external QE, compared to commercial phosphors, such as $Si_{6-z}Al_zO_zN_{8-z}:Eu^{2+}$ and $Ca_3Sc_2Si_3O_{12}:Ce^{3+}$. Moreover, high Ce-content seemingly prevents the formation of the CMSL host. However, the mechanism of phase transformation should be studied in detail.

4. Conclusions

A novel broad band green-yellow emitting orthosilicate phosphor $Ca_{1.5}Mg_{0.5}Si_{1-x}Li_xO_{4-\delta}:Ce^{3+}$ (CMSL:Ce) was successfully produced. The experimental results showed that Li^+ occupies the Si^{4+} sites in silicates. This substitution is reported for the first time and seems to play a key role in the development of the novel phase, whose formation mechanism is governed by a phase transformation. This phase transformation takes place with a volume expansion of 13.81%, leading to a spontaneous total cracking of the hard sintered lump of $Ca_3MgSi_2O_8$ into a fine powder of CMSL. Under excitation with UV light at 365 nm and violet light at 410 nm, the produced phosphor produces green-yellow emission with a peak at ~500 nm and an FWHM of ~120 nm. The novel phosphor displays high QE and good thermal quenching properties. Nevertheless, both these properties can apparently be improved considerably if the purity of the produced phosphor is also improved (*i.e.* to be free from the impurity phase $Ca_3MgSi_2O_8$) and, provided that this is accomplished, production of single phase CMSL:Ce phosphors will be achieved.

White-light-emitting diodes with high CRI (R_a = 92.8) were produced by combining a 365 nm emitting chip with blue-emitting $BaMgAl_{10}O_{17}:Eu^{2+}$, green-yellow emitting CMSL:0.01Ce, and red-emitting $Sr_2Si_5N_8:Eu^{2+}$phosphors.

Consequently, the results of this study qualify the produced novel phosphor for further consideration and experimentation as a green-yellow emitting phosphor potentially suitable for illumination application.

Conflicts of interest

There are no conflicts to declare.

Acknowledgements

This research was supported by the National Science Foundation of China (51372238, 11435012, 51572023 and 91622125) and the CNPC-CAS Strategic Cooperation Research Program (2015A-4812). The authors thank the BL14W1 beamline of Shanghai Synchrotron Radiation Facility for the XAFS measurements and the Frank Laboratory for Neutron Physics (Russia) for the T.O.F. neutron diffraction measurements.

References

1 H. Zhu, C. C. Lin, W. Luo, S. Shu, Z. Liu, Y. Liu, J. Kong, E. Ma, Y. Cao and R.-S. Liu, *Nat. Commun.*, 2014, **5**, 4312.
2 T. Takeda, N. Hirosaki, S. Funahshi and R.-J. Xie, *Chem. Mater.*, 2015, **27**, 5892–5898.
3 X.-J. Wang, L. Wang, T. Takeda, S. Funahashi, T. Suehiro, N. Hirosaki and R.-J. Xie, *Chem. Mater.*, 2015, **27**, 7689–7697.
4 Z. Xia, C. Ma, M. S. Molokeev, Q. Liu, K. Rickert and K. R. Poeppelmeier, *J. Am. Chem. Soc.*, 2015, **137**, 12494–12497.
5 A. Birkel, K. A. Denault, N. C. George, C. E. Doll, B. Héry, A. A. Mikhailovsky, C. S. Birkel, B.-C. Hong and R. Seshadri, *Chem. Mater.*, 2012, **24**, 1198–1204.
6 J. Ueda, P. Dorenbos, A. J. J. Bos, A. Meijerink and S. Tanabe, *J. Phys. Chem. C*, 2015, **119**, 25003–25008.
7 Z. Xia and R.-S. Liu, *J. Phys. Chem. C*, 2012, **116**, 15604–15609.
8 N. Komuro, M. Mikami, Y. Shimomura, E. G. Bithell and A. K. Cheetham, *J. Mater. Chem. C*, 2015, **3**, 204–210.
9 Y. Shimomura, T. Honma, M. Shigeiwa, T. Akai, K. Okamoto and N. Kijima, *J. Electrochem. Soc.*, 2007, **154**, J35–J38.
10 R.-J. Xie, N. Hirosaki, H.-L. Li, Y. Li and M. Mitomo, *J. Electrochem. Soc.*, 2007, **154**, J314–J319.
11 M. Seibald, T. Rosenthal, O. Oeckler, C. Maak, A. Tücks, P. J. Schmidt, D. Wiechert and W. Schnick, *Chem. Mater.*, 2013, **25**, 1852–1857.
12 K. A. Denault, J. Brgoch, M. W. Gaultois, A. Mikhailovsky, R. Petry, H. Winkler, S. P. DenBaars and R. Seshadri, *Chem. Mater.*, 2014, **26**, 2275–2282.
13 X.-J. Wang, L. Wang, T. Takeda, S. Funahashi, T. Suehiro, N. Hirosaki and R.-J. Xie, *Chem. Mater.*, 2015, **27**, 7689–7697.
14 S. Schmiechen, H. Schneider, P. Wagatha, C. Hecht, P. J. Schmidt and W. Schnick, *Chem. Mater.*, 2014, **26**, 2712–2719.
15 S. Schmiechen, P. Strobel, C. Hecht, T. Reith, M. Siegert, P. J. Schmidt, P. Huppertz, D. Wiechert and W. Schnick, *Chem. Mater.*, 2015, **27**, 1780–1785.
16 T. Takeda, N. Hirosaki, S. Funahshi and R.-J. Xie, *Chem. Mater.*, 2015, **27**, 5892–5898.
17 L.-C. Ju, C. Cai, Q.-Q. Zhu, J.-Y. Tang, L.-Y. Hao and X. Xu, *J. Mater. Sci.: Mater. Electron.*, 2013, **24**, 4516–4521.
18 A. Kalaji, M. Mikami and A. K. Cheetham, *Chem. Mater.*, 2014, **26**, 3966–3975.
19 Y. Sato, H. Kato, M. Kobayashi, T. Masaki, D. H. Yoon and M. Kakihana, *Angew. Chem., Int. Ed.*, 2014, **53**, 7756–7759.
20 W. Ji, M.-H. Lee, L. Hao, X. Xu, S. Agathopoulos, D. Zheng and C. Fang, *Inorg. Chem.*, 2015, **54**, 1556–1562.
21 W. Ji, S. Ye, M.-H. Lee, L. Hao, X. Xu, S. Agathopoulos, D. Zheng, C. Fang and Y. Huang, *J. Mater. Chem. C*, 2016, **4**, 3313–3320.

22 Z. Xia, G. Liu, J. Wen, Z. Mei, M. Balasubramanian, M. S. Molokeev, L. Peng, L. Gu, D. J. Miller, Q. Liu and K. R. Poeppelmeier, *J. Am. Chem. Soc.*, 2016, **138**, 1158–1161.
23 K. A. Denault, J. Brgoch, M. W. Gaultois, A. Mikhailovsky, R. Petry, H. Winkler, S. P. DenBaars and R. Seshadri, *Chem. Mater.*, 2014, **26**, 2275–2282.
24 Y. Li, A. Delsing, G. De With and H. Hintzen, *Chem. Mater.*, 2005, **17**, 3242–3248.
25 H. S. Jang, H. Y. Kim, Y.-S. Kim, H. M. Lee and D. Y. Jeon, *Opt. Express*, 2012, **20**, 2761–2771.
26 V. ShelXTL, Inc., Madison, WI, 1994.
27 TOPAS V4.2: General profile and structure analysis software for powder diffraction data, User's Manual, Bruker AXS, Karlsruhe, Germany, 2008.
28 K. Ohkubo and T. Shigeta, *J. Illum. Eng. Inst. Japan*, 1999, **83**, 87–93.
29 H. Lihui, Z. Xiao and L. Xingren, *J. Alloys Compd.*, 2000, **305**, 14–16.
30 H. Schulz and V. Tscherry, *Acta Crystallogr., Sect. B: Struct. Crystallogr. Cryst. Chem.*, 1972, **28**, 2174–2177.
31 Z. Xu and J. F. Stebbins, *Solid State Nucl. Magn. Reson.*, 1995, **5**, 103–112.
32 T. M. Anderson, S. G. Thoma, F. Bonhomme, M. A. Rodriguez, H. Park, J. B. Parise, T. M. Alam, J. P. Larentzos and M. Nyman, *Cryst. Growth Des.*, 2007, **7**, 719–723.
33 M. Vijayakumar, S. Kerisit, Z. Yang, G. L. Graff, J. Liu, J. A. Sears, S. D. Burton, K. M. Rosso and J. Hu, *J. Phys. Chem. C*, 2009, **113**, 20108–20116.
34 C. J. Chan, W. M. Kriven and J. F. Young, *J. Am. Ceram. Soc.*, 1992, **75**, 1621–1627.
35 S.-i. Nishimura, G. Kobayashi, K. Ohoyama, R. Kanno, M. Yashima and A. Yamada, *Nat. Mater.*, 2008, **7**, 707–711.
36 R. t. Shannon, *Acta Crystallogr., Sect. A: Cryst. Phys., Diffr., Theor. Gen. Crystallogr.*, 1976, **32**, 751–767.
37 F. Yu, Y. Wang, J. Wang and Z. Xie, *Physicochem. Probl. Miner. Process.*, 2014, **50**, 535–550.
38 M. E. Stournara and V. B. Shenoy, *J. Power Sources*, 2011, **196**, 5697–5703.
39 B. Cordero, V. Gomez, A. E. Platero-Prats, M. Reves, J. Echeverria, E. Cremades, F. Barragan and S. Alvarez, *Dalton Trans.*, 2008, 2832–2838.
40 L.-C. Ju, X. Xu, L.-Y. Hao, Y. Lin and M.-H. Lee, *J. Mater. Chem. C*, 2015, **3**, 1567–1575.
41 N. Hirosaki, R.-J. Xie, K. Kimoto, T. Sekiguchi, Y. Yamamoto, T. Suehiro and M. Mitomo, *Appl. Phys. Lett.*, 2005, **86**, 211905.
42 Y. F. Wu, Y. H. Chan, Y. T. Nien and I. G. Chen, *J. Am. Ceram. Soc.*, 2013, **96**, 234–240.
43 L. Wang, R.-J. Xie, T. Suehiro, T. Takeda and N. Hirosaki, *Chem. Rev.*, 2018, **118**, 1951–2009.